Supplemental Material

for

Unveiling the Influence of Boron Clathrate Lattice on Superconductivity in Ternary Mg-La-B System

Yiming Zhang, Meiling Xu*, Jian Hao and Yinwei Li*

Laboratory of Quantum Functional Materials Design and Application, School of Physics and Electronic Engineering, Jiangsu Normal University, Xuzhou 221116, China

Corresponding authors: xml@calypso.cn and yinwei_li@jsnu.edu.cn

Supplemental Computational Methods

Universal variable-composition structure searches for $MgLaB_x$, Mg_2LaB_x, and $MgLa_2B_x$, wherein x ranges from 1 to 18, were performed at 0 and 50 GPa with the CALYPSO structure prediction method[1–5], which requires only chemical compositions for given compounds to predict stable or metastable structures at a given pressure, using simulation cells that consist of a maximal number of 36 atoms. For maximum prediction efficiency, we employed particle swarm optimization (PSO) technology alongside symmetry constraints during structural generation. Using this method, child structures were generated based on the current optimal structure. In total, we examined 54 unique compositions at each pressure, which entailed analyzing approximately 400 structures for each stoichiometry. For 10 compositions with a formation enthalpy below 140 meV/atom, as compared to the most competitive elements, binaries, and ternaries, we performed additional fixed-composition structural predictions until convergence was reached. This involved generating up to 3000 structures for each stoichiometry.

The structural relaxations and electronic structure calculations are performed based on density functional theory[6] as implemented in the Vienna ab initio simulations package (VASP)[7]. The Perdew-Burke-Ernzerhof generalized gradient approximation[8] is chosen for the exchange-correlation function. The electron-ion interactions are considered by the projector-augmented-wave potentials[9], with $3s^2$, $5s^25p^65d^16s^2$, and $2s^22p^1$ configurations as valence electrons for Mg, La, and B atoms, respectively. Plane-wave cutoff energy of 600 eV and Monkhorst–Pack k meshes[10] with a grid spacing of

$2\pi \times 0.02$ Å^{-1} are adopted. The energy and force convergence precisions are 10^{-6} eV and 0.01 eV Å^{-1}, respectively. *Ab initio* molecular dynamics (AIMD) simulations are performed using the Nosé–Hoover chain thermostat[11] for 20 ps with a time step of 1 fs. The simulation supercell had dimensions of 2×1×1 cell at 50 GPa and 2×2×2 cell at 0 GPa, containing a total of 192 atoms.

The phonon spectra and EPC are calculated within density functional perturbation theory[12] using the QUANTUM ESPRESSO code[13]. Ultrasoft pseudopotentials[14] are used to model the electron-ion interactions. The kinetic energy cutoffs for wavefunctions and charge density are chosen to be 80 Ry and 800 Ry, respectively. The convergence of the EPC parameter, λ, versus the Gaussian spreading, σ, for $MgLaB_{10}$ at 0 GPa was tested at the Γ point using various k grids as shown in Fig. S01(a). The EPC parameter, λ, was determined utilizing a series of Gaussian broadenings, with increments of 0.005 Ry from 0.005 Ry to 0.050 Ry. Our findings reveal that the utilization of a 16 × 16 × 8 *k*-point grid achieves satisfactory convergence at σ = 0.030 Ry, when combined with 4 × 4 × 2 *q*-point grid (corresponding to 14 *q* points). In order to establish the convergence of the T_c with respect to the *q*-point grid, supplementary calculations were executed employing an expanded *q*-point grid of 5 × 5 × 2 (corresponding to 18 *q* points), as displayed in Fig. S01(b). The resulting T_c values are 19.85 K and 20.07 K using 4 × 4 × 2 and 5 × 5 × 2 *q*-point grids, respectively. Thus, considering the balance between computational precision and efficiency, we conclude that the adoption of 4 × 4 × 2 *q*-point grids is reasonable and appropriate for conducting accurate EPC calculations. Given the 48-atom unit cell of $MgLaB_{10}$ at 50 GPa, a 2 × 2 × 2 k-point grid combined with a 1 × 1 × 1 *q*-point grid was used to estimate T_c. The T_c is estimated based on the Allen–Dynes-modified McMillan equation[15], with a typical choice of Coulomb pseudopotential of $\mu^* = 0.1$.

We employ the EPW code[16–18] for the superconducting gap and EPC, and the WANNIER90 code[19] for generating maximally localized Wannier functions (MLWFs). Electronic wave functions and dynamical matrices required for the Wannier interpolations are calculated within a uniform *k*-mesh of 16 × 16 × 8 and *q*-mesh of 4 × 4 × 2, respectively. Thirty orbitals, *p* orbitals for each B atom, are used to describe the

electronic structure with MLWFs. Eventually, the *k*-point grid of 64 × 64 × 32 and the *q*-point grid of 16 × 16 × 8 are adopted to interpolate the EPC quantities. The fermion Matsubara frequency cutoff is set to be 1.2 eV, which is 10 times the largest phonon frequency. The width of the Fermi surface window is set at 0.2 eV. Dirac δ functions for electrons and phonons are replaced by Lorentzians of widths 50 meV and 0.5 meV, respectively. The consistency of band structures obtained by Wannier interpolation and first-principles calculations can be found in Fig. S02, generating a solid foundation for subsequent EPW calculation.

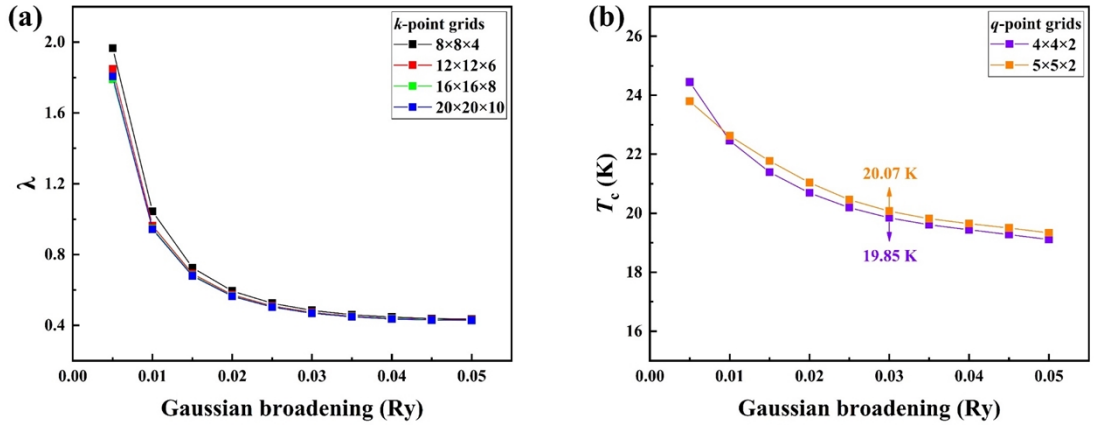

FIG. S01 (a) Electron-phonon coupling constant, λ, versus Gaussian broadening, σ, for $MgLaB_{10}$ at 0 GPa at the Γ point using various *k*-point grids. (b) The values of T_c versus Gaussian broadening, σ, for $MgLaB_{10}$ at 0 GPa using 4 × 4 × 2 and 5 × 5 × 2 *q*-point grids.

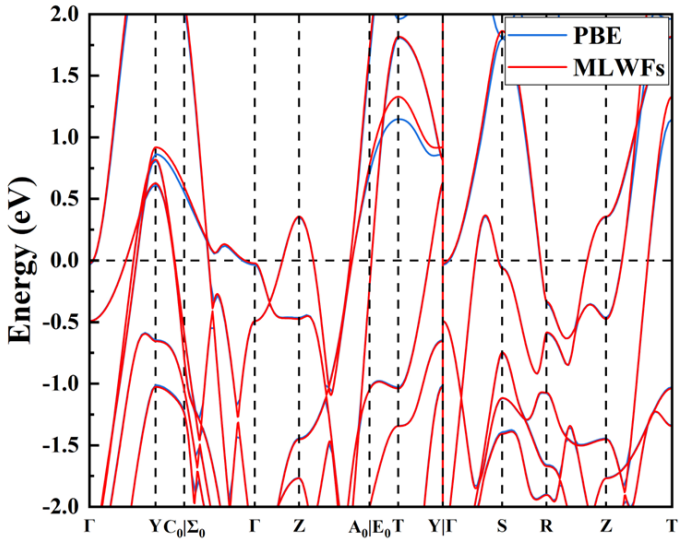

FIG. S02 Band structures of $MgLaB_{10}$ are given by first-principles calculation and by interpolation of maximally localized Wannier functions (MLWFs).

The calculation of Fermi surface nesting function employs 180 *k* points and 280 *q*

points to attain their respective energy eigenvalues. The nesting function[20–22]

$$\xi(Q) = \frac{1}{N}\sum_{\vec{k},i,j} \delta\left(\varepsilon_{\vec{k},i} - \varepsilon_F\right)\delta\left(\varepsilon_{\vec{k}+\vec{Q},j} - \varepsilon_F\right),$$

where $\varepsilon_{k,i}$ is the Kohn-Sham eigenvalue and i, j are the indices of energy bands, N is the number of k points, and ε_F is the Fermi energy. To calculate the $\xi(Q)$, we used the density function of normal distribution (i.e., Gaussian function) to replace the δ function with the broadening of 0.05.

The temperature-dependent formation Gibbs free energy for the specified decomposition reactions can be calculated by considering the vibrational contributions through the quasi-harmonic approximation. Two distinct sets of calculations were conducted. Initially, phonon dispersions and the corresponding phonon density of states (PhDOS) were computed using the direct supercell method, implemented in the PHONOPY code. The resulting PhDOS served as input for determining the vibrational contribution to the entropy for each phase. Subsequently, the Gibbs free energies of the relevant phases were computed by combining these results with the total internal energy, pressure, and volume obtained from the VASP calculations.

Supplemental Tables

TABLE S1. Structural parameters of Mg-La-B compounds with the formation energies < 140 meV/atom at 0 GPa and 50 GPa.

Compound	Pressure (GPa)	Space group	*a*, *b*, *c* (Å) *α*, *β*, *γ* (deg)	Atomic position
MgLaB	0	*Cmcm*	*a*=3.826 *b*=21.209 *c*=3.231	Mg1(4c) (0.000, 0.292, 1.250) La1(4c) (0.500, 0.416, 0.750) B1(4c) (0.000, 0.489, 1.250)
$MgLa_2B_2$	0	*Cmmm*	*a*=3.223 *b*=17.752 *c*=3.817	Mg1(2c) (0.500, 0.000, 0.500) La1(4i) (0.500, 0.650, 0.000) B1(4j) (0.000, 0.736, 0.500)

$MgLaB_2$	0	*C*2/*m*	*a*=9.054 *b*=4.436 *c*=8.47 *β*=116.94	Mg1(4i) (0.373, 0.500, 0.067) La1(4i) (0.841, 0.500, 0.698) B1(4i) (0.474, 0.500, 0.592) B3(4h) (0.500, 0.817, 0.500)
$MgLa_2B_6$	0	*P*4/*mmm*	*a*=*b*=4.168 *c*=7.650	Mg1(1a) (0.000, 0.000, 0.000) La1(2h) (0.500, 0.500, 0.734) B1(2g) (0.000, 0.000, 0.670) B3(4m) (0.000, 0.700, 0.500)
$MgLaB_8$	0	*Pmma*	*a*=5.676 *b*=4.048 *c*=8.980	Mg1(2f) (0.250, 0.500, 0.067) La1(2f) (0.250, 0.500, 0.668) B1(4k) (-0.250, 0.702, 0.669) B5(4i) (-0.087, 0.000, 0.766) B7(4i) (-0.095, 0.000, 0.081) B9(4i) (0.404, 0.000, 0.431)
$MgLaB_{10}$	0	*Cmmm*	*a*=5.008 *b*=7.546 *c*=5.611	Mg1(2b) (0.500, 0.000, 0.000) La1(2d) (0.000, 0.000, -0.500) B1(8m) (0.250, -0.250, -0.167) B2(8n) (0.500, -0.135, -0.652) B9(4i) (0.500, -0.385, 0.000)
$MgLaB_{12}$	0	*P*4*mm*	*a*=*b*=5.871 *c*=4.186	Mg1(1a) (0.000, 0.000, 0.096) La1(1b) (0.500, 0.500, 0.826) B1(2c) (0.000, 0.500, 0.027) B3(2c) (0.000, 0.500, 0.628) B5(8g) (0.850, 0.648, 0.330)
$MgLa_2B_4$	50	*R*-3*m*	*a*=*b*=3.012 *c*=27.798	Mg1(3b) (0.000, 0.000, 0.500) La1(6c) (0.000, 0.000, 0.376) B1(6c) (0.000, 0.000, 0.112) B3(6c) (0.000, 0.000, 0.778)
$MgLaB_4$	50	*Cmmm*	*a*=5.008 *b*=7.546 *c*=5.611	Mg1(4i) (0.000, 0.321, 0.000) La1(4g) (0.800, 0.000, 0.000) B1(8q) (0.658, 0.776, 0.500) B2(4j) (0.000, 0.123, 0.500) B3(4h) (0.591, 0.000, 0.500)
$MgLaB_8$	50	*Pmma*	*a*=5.505 *b*=3.747 *c*=7.718	Mg1(2a) (0.000, 0.000, 0.000) La1(2e) (0.250, 0.000, -0.637) B1(4k) (0.250, 0.212, -0.277) B2(2f) (0.250, 0.500, -0.094) B4(2f) (0.250, 0.500, -0.885) B7(4j) (0.988, 0.500, -0.787) B10(4j) (0.095, 0.500, -0.419)
$MgLaB_{10}$	50	*Cmmm*	*a*=14.229 *b*=9.148 *c*=5.376	Mg1(2a) (0.000, 0.000, 0.000) Mg2(2b) (0.000, -0.500, 0.000) Mg3(4e) (0.250, -0.250, 0.000)

	La1(4h) (0.255, -0.500, 0.500)
	La3(4j) (0.000, -0.751, 0.500)
	B1(16r) (-0.130, -0.609, 0.171)
	B9(16r) (-0.121, -0.134, 0.168)
	B17(16r) (-0.184, -0.744, 0.653)
	B25(8o) (-0.433, -0.500, 0.655)
	B29(8o) (0.061, -0.500, 0.651)
	B33(4g) (-0.318, -0.500, 0.000)
	B35(4g) (0.205, -0.500, 0.000)
	B37(8p) (-0.057, -0.735, 0.000)

TABLE S2. Summaries of total DOSs and atom-projected DOSs values (in the unit of states/eV/f.u.) at the Fermi level of the Mg-La-B compounds.

Compounds	Pressures (GPa)	$N(E_F)_{total}$	$N(E_F)_{Mg}$	$N(E_F)_{La}$	$N(E_F)_{B}$
MgLaB	0	0.70	0.07	0.54	0.09
$MgLa_2B_2$	0	1.45	0.10	1.18	0.17
$MgLaB_2$	0	0.56	0.08	0.32	0.16
$MgLa_2B_6$	0	1.18	0.06	0.69	0.43
$MgLaB_8$-I	0	0.62	0.02	0.27	0.33
$MgLaB_{12}$	0	0.71	0.02	0.33	0.36
$MgLa_2B_4$	0	1.72	0.02	1.41	0.29
$MgLaB_4$	0	0.59	0.04	0.23	0.32
$MgLaB_8$-II	0	0.71	0.04	0.30	0.37
$MgLaB_{10}$	0	1.52	0.08	0.18	1.26
$MgLa_2B_4$	50	1.80	0.03	1.36	0.41
$MgLaB_4$	50	0.80	0.05	0.29	0.46
$MgLaB_8$-II	50	0.59	0.02	0.25	0.32
$MgLaB_{10}$	50	1.42	0.02	0.19	1.21

TABLE S3. Bader charges in $MgLaB_{10}$ at 0 GPa. Positive and negative represent electron gain and loss, respectively.

Compound	Mg	La	B
$MgLaB_{10}$	-1.60	-1.68	+0.33

TABLE S4. Comparison of the total/B-derived DOSs at the Fermi level, EPC constant λ, and superconductivity of $MgLaB_{10}$ with other boron clathrate superconductors at ambient pressure.

Compounds	$N(E_F)_{total}$ (states/eV/f.u.)	$N(E_F)_B$ (states/eV/f.u.)	λ	T_c (K)	Refs
$MgLaB_{10}$	1.52	1.26	0.83	20.0	This work
LaB_8	1.04	0.90	0.66	14.0-19.6	[23,24]
$LiLaB_8$	0.65	0.45	0.63	9.5	[25]
CaB_7	0.64	0.57	0.50	7.7	[26]

TABLE S5. Comparison of the total DOS at the Fermi level, the logarithmic frequency average ω_{log}, zone-center EPC constant λ_Γ, EPC constant λ and superconductivity of $MgLaB_{10}$, $MgLa_2B_6$, $MgLaB_8$-I, $MgLaB_{12}$ and $MgLaB_4$.

Compounds	Pressure (GPa)	$N(E_F)_{total}$ (states/eV/f.u.)	ω_{log} (K)	λ_Γ	λ	T_c (K)
$MgLaB_{10}$	0	1.52	391	0.17	0.83	20.0
	50	1.42	401	0.25	0.80	19.0
$MgLa_2B_6$	0	1.18	173	0.09	0.46	1.5
$MgLaB_8$-I	0	0.62	365	0.08	0.31	0.2
$MgLaB_{12}$	0	0.71	316	0.05	0.27	0.1
$MgLaB_4$	0	0.59	428	0.10	0.47	4.0

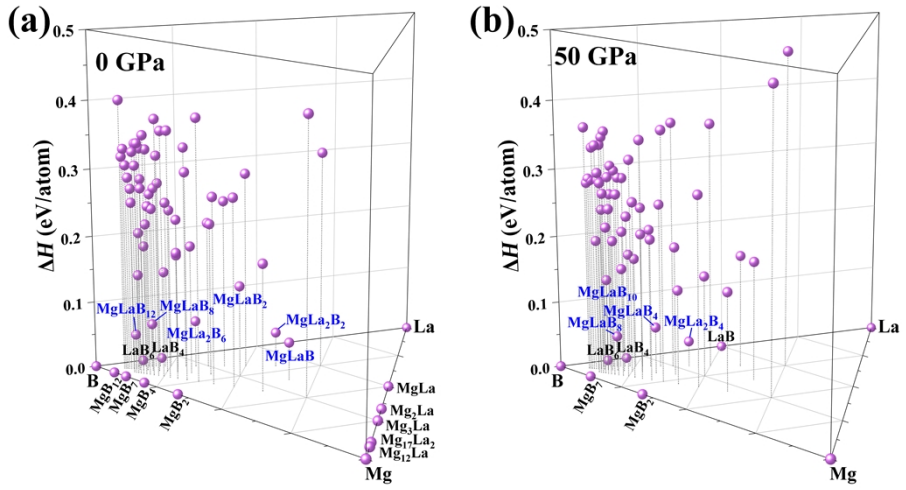

Supplemental Figures

FIG. S1 Calculated 3D convex hull of the ternary Mg-La-B system at (a) 0 and (b) 50 GPa.

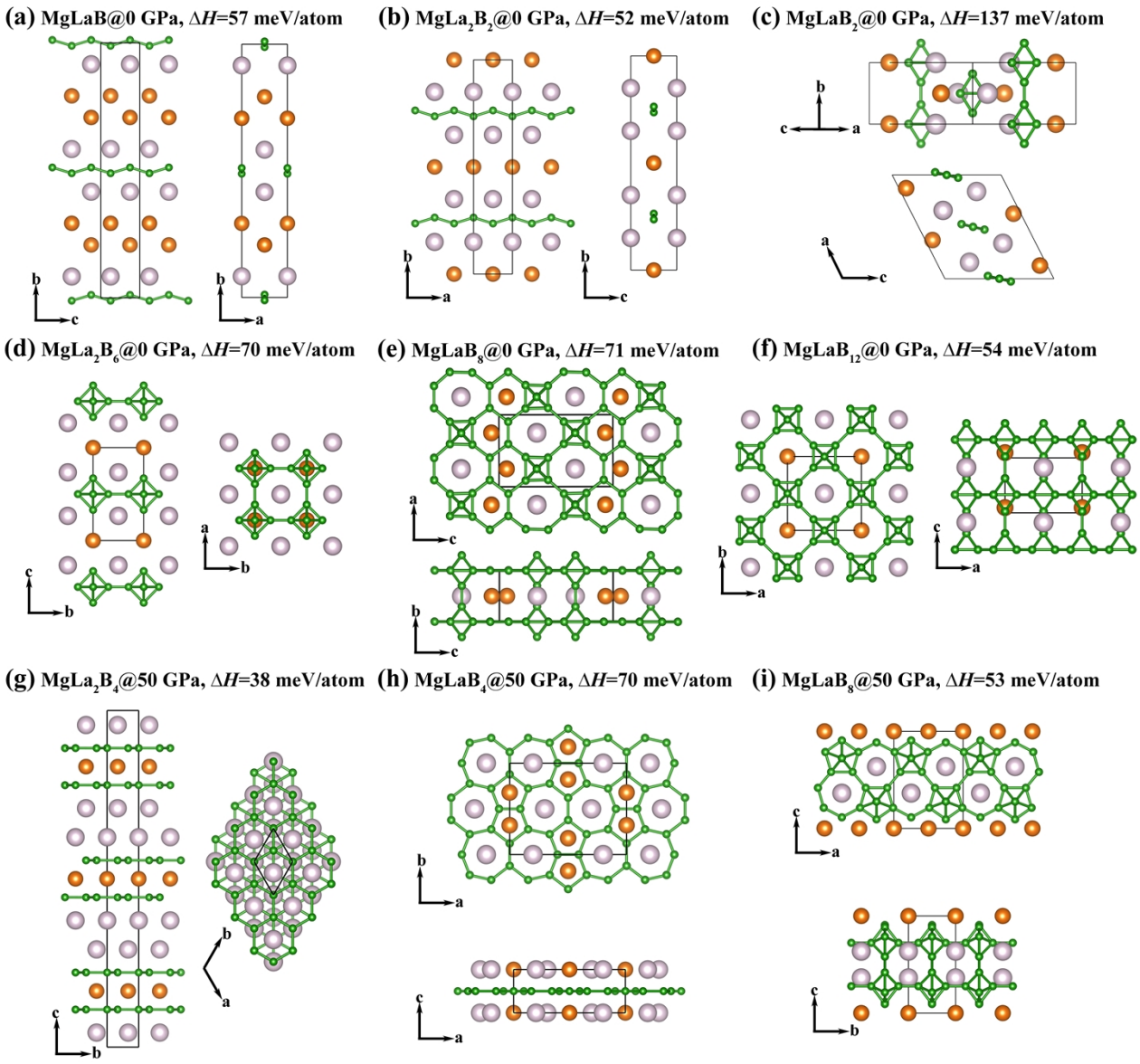

FIG. S2 The crystal structures and formation enthalpies of (a) *Cmcm* MgLaB at 0 GPa, (b) *Cmmm* $MgLa_2B_2$ at 0 GPa, (c) *C*2/*m* $MgLaB_2$ at 0 GPa, (d) *P*4/*mmm* $MgLa_2B_6$ at 0 GPa, (e) *Pmma* $MgLaB_8$ at 0 GPa, (f) *P*4*mm* $MgLaB_{12}$ at 0 GPa, (g) *R*-3*m* $MgLa_2B_4$ at 50 GPa, (h) *Cmmm* $MgLaB_4$ at 50 GPa and (i) *Pmma* $MgLaB_8$ at 50 GPa. The orange, pink, and green spheres represent Mg, La, and B atoms, respectively.

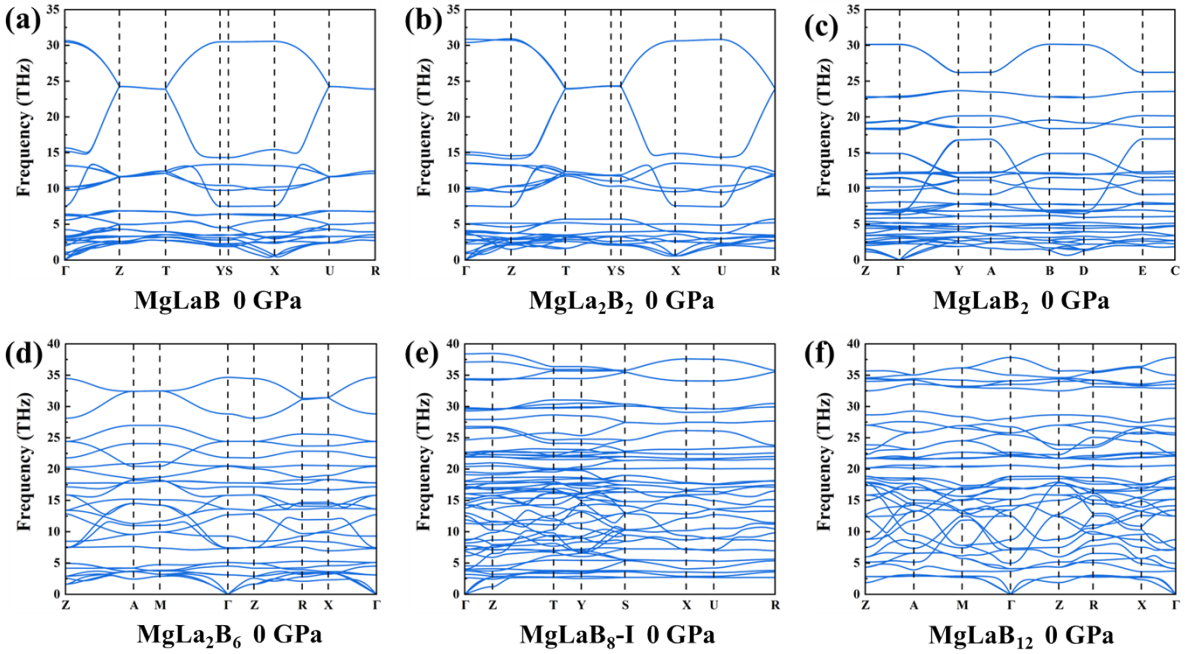

FIG. S3 Phonon spectra of Mg-La-B compounds with the formation energies < 140 meV/atom predicted at ambient pressure.

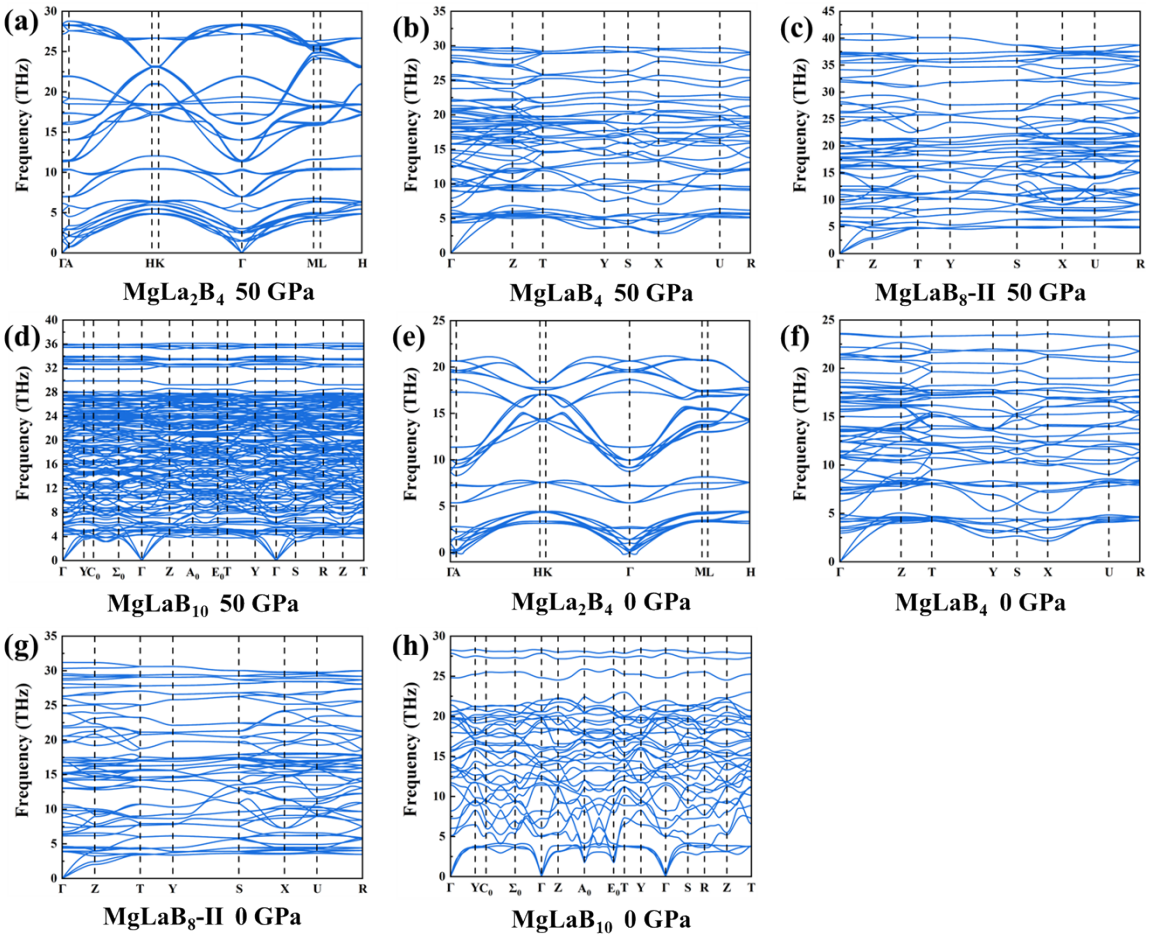

FIG. S4 (a-d) Phonon spectra of Mg-La-B compounds with the formation energies < 140 meV/atom predicted at 50 GPa. (e-h) Phonon spectra of pressure-induced Mg-La-B compounds at 0 GPa.

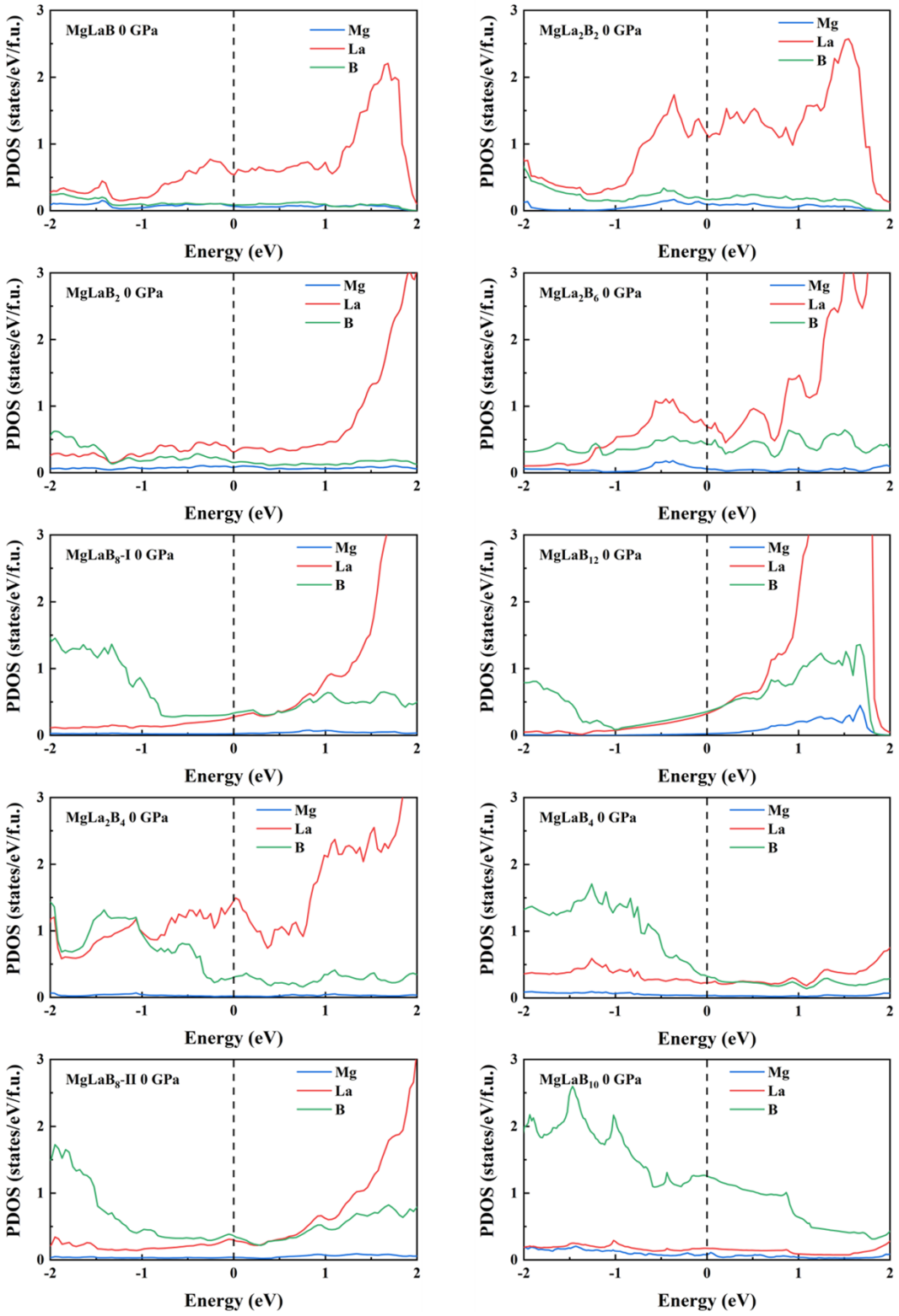

FIG. S5 Atom-projected density of states of Mg-La-B compounds with the formation energies < 140 meV/atom at 0 GPa.

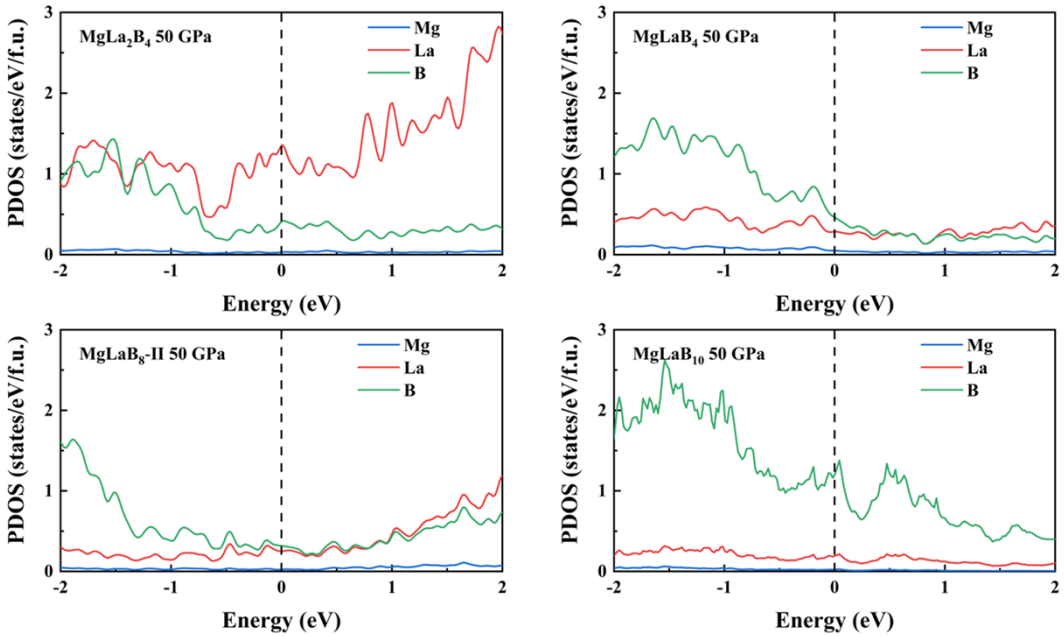

FIG. S6 Atom-projected density of states of the Mg-La-B compounds with the formation energies < 140 meV/atom at 50 GPa.

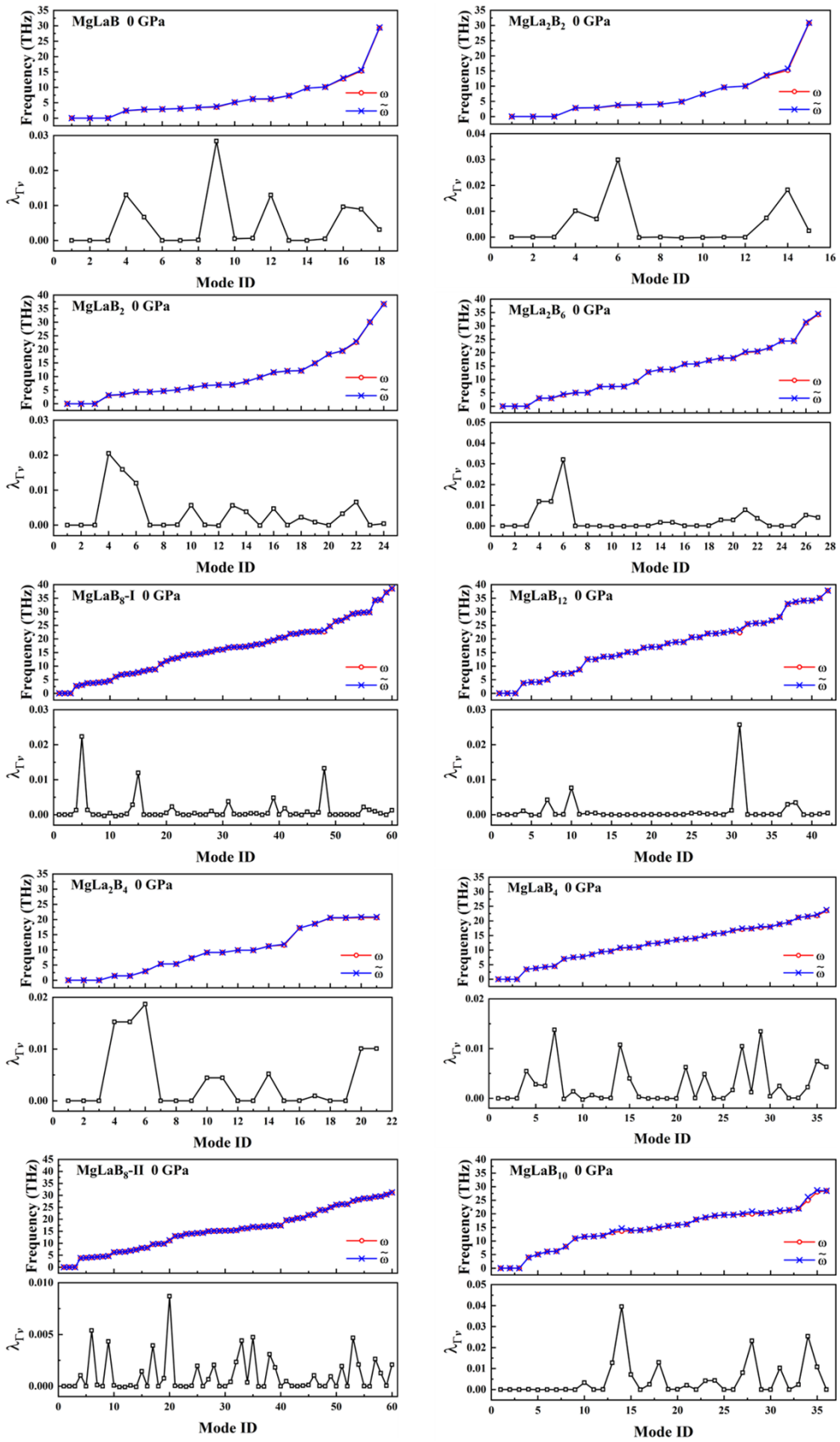

FIG. S7 The screened and unscreened phonon frequency (top panel) and zone-center EPC strength (bottom panel) of the Mg-La-B compounds with the formation energies < 140 meV/atom at 0 GPa.

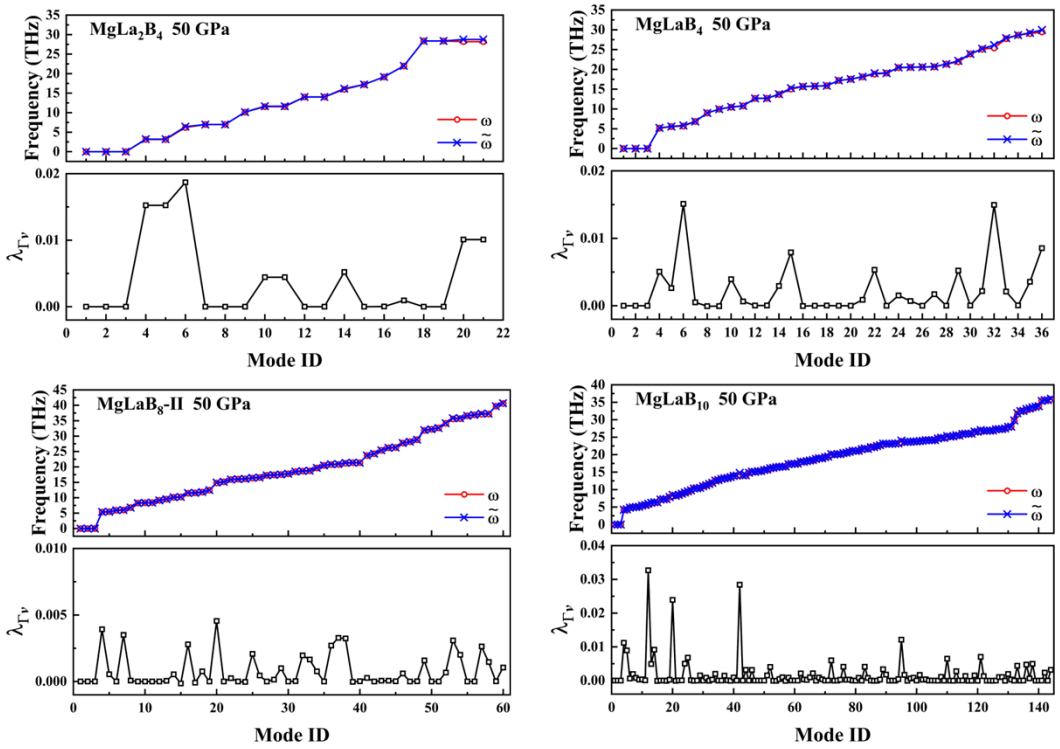

FIG. S8 The screened and unscreened phonon frequency (top panel) and zone-center EPC strength (bottom panel) of Mg-La-B compounds with the formation energies < 140 meV/atom at 50 GPa.

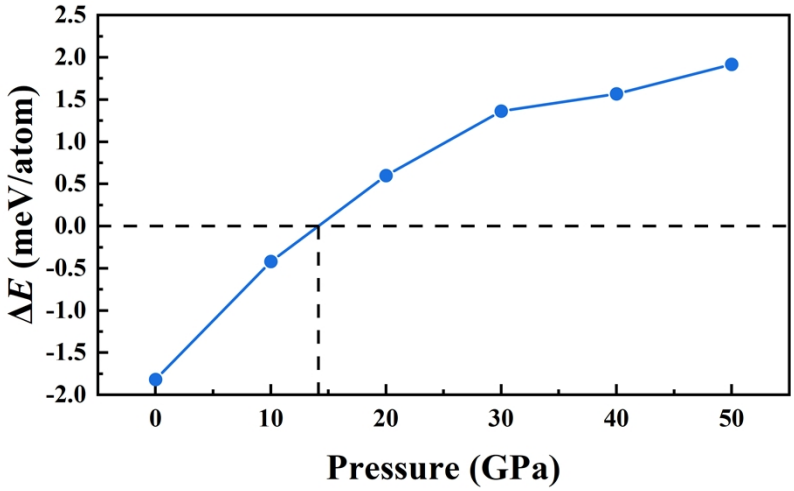

FIG. S9 The enthalpy difference between two $MgLaB_{10}$ compounds.

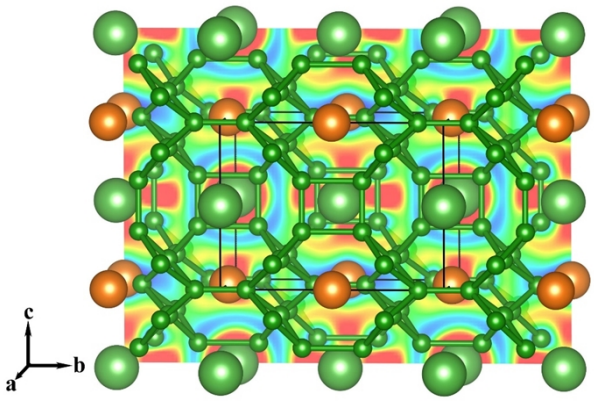

FIG. S10 Electron localization function (ELF) along the (100) plane of *Cmmm* $MgLaB_{10}$ at 0 GPa with the isosurface level of 0.8.

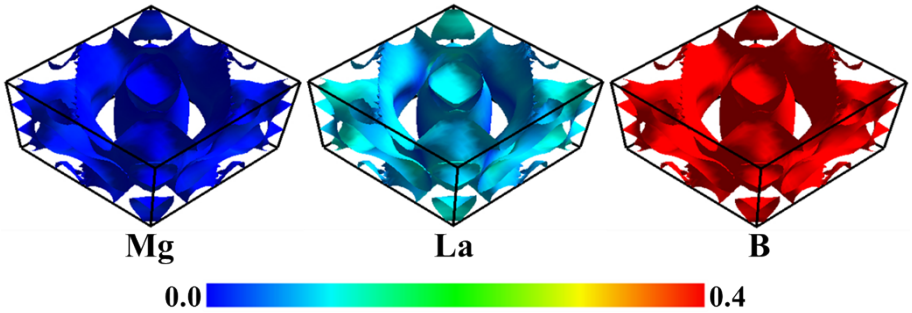

FIG. S11 Fermi surfaces of $MgLaB_{10}$ in the primitive BZ. The electronic state at each FS sheet is respectively projected onto Mg, La, and B atoms using the color scale in the range [0, 0.4].

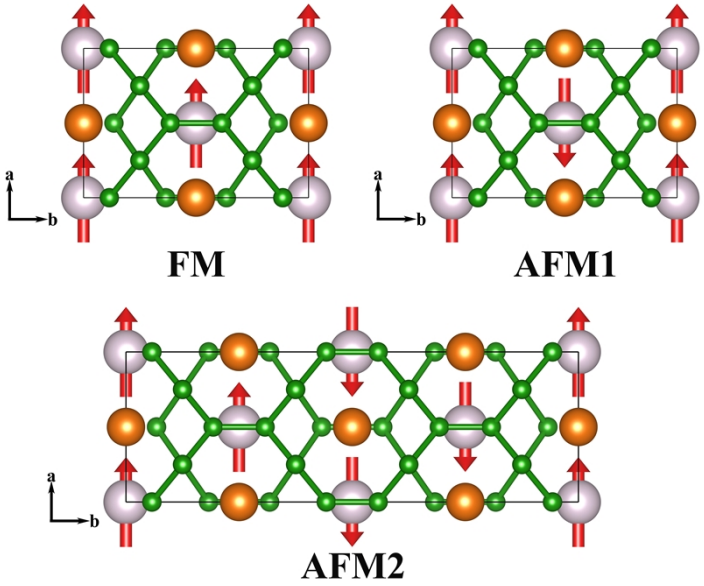

FIG. S12 Three possible magnetic configurations of $MgLaB_{10}$. The orange, pink, and green spheres represent Mg, La, and B atoms, respectively. The red arrows represent the spin directions of La atoms.

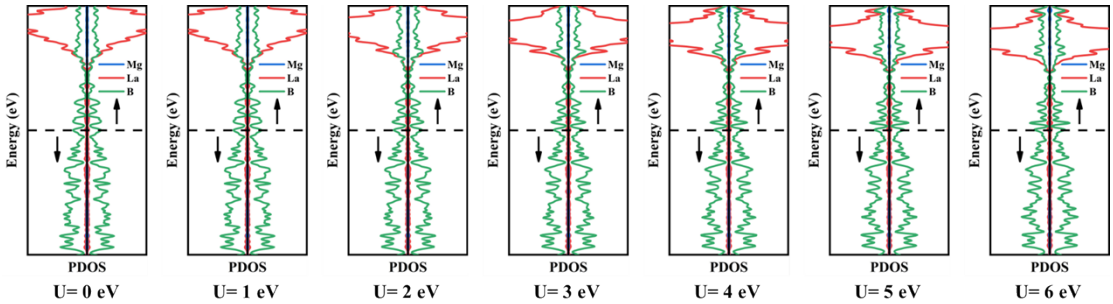

FIG. S13 PDOSs of $MgLaB_{10}$ with inclusion of different Hubbard U parameters.

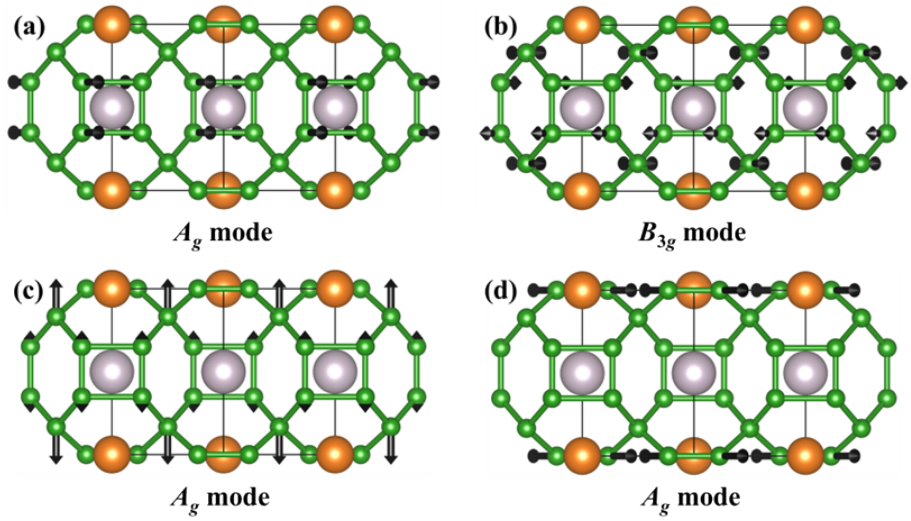

FIG. S14 Vibrational patterns for the phonon modes (a) 14, (b) 18, (c) 28 and (d) 34 with black arrows indicating the atomic vibration direction.

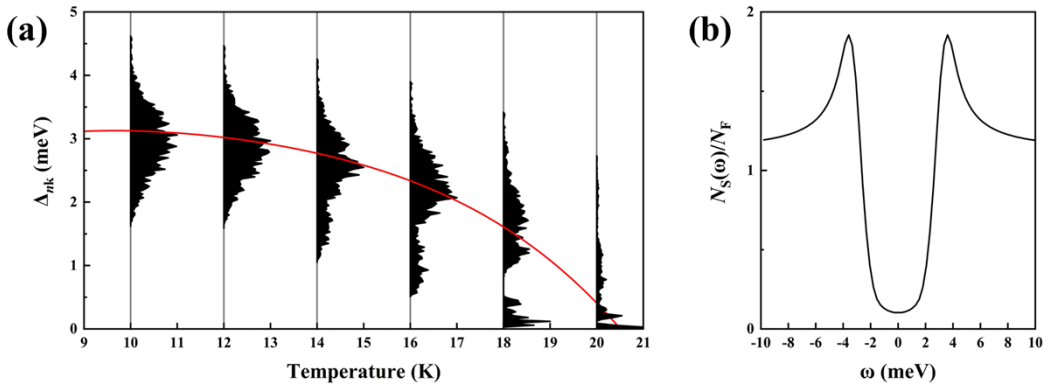

FIG. S15 (a) Energy distribution of superconducting gaps Δ_{nk} versus temperature for $MgLaB_{10}$ at 0 GPa. The red solid line represents the average value of the entire anisotropic single gap. (b) SDOS at 10 K for $MgLaB_{10}$.

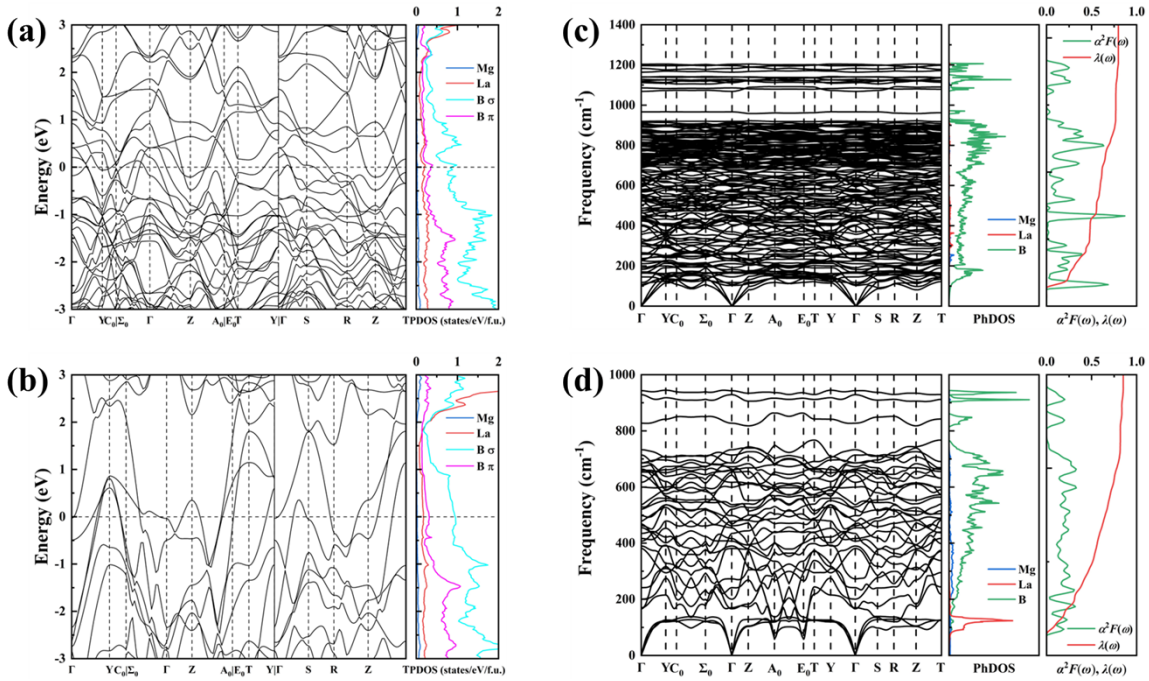

FIG. S16 Electronic band structure and the projected density of states (PDOS) of $MgLaB_{10}$ at (a) 50 and (b) 0 GPa. Phonon dispersion relations, projected phonon density of states (PhDOS), Eliashberg function $\alpha^2F(\omega)$, and integrated electron–phonon coupling strength $\lambda(\omega)$ of $MgLaB_{10}$ at (c) 50 and (d) 0 GPa.

References

1 Y. Wang, J. Lv, L. Zhu and Y. Ma, *Phys. Rev. B*, 2010, **82**, 094116.

2 Y. Wang, M. Miao, J. Lv, L. Zhu, K. Yin, H. Liu and Y. Ma, *J. Chem. Phys.*, 2012, **137**, 224108.

3 Y. Wang, J. Lv, L. Zhu and Y. Ma, *Comput. Phys. Commun.*, 2012, **183**, 2063–2070.

4 B. Gao, P. Gao, S. Lu, J. Lv, Y. Wang and Y. Ma, *Sci. Bull.*, 2019, **64**, 301–309.

5 X. Shao, J. Lv, P. Liu, S. Shao, P. Gao, H. Liu, Y. Wang and Y. Ma, *J. Chem. Phys.*, 2022, **156**, 014105.

6 W. Kohn and L. J. Sham, *Phys. Rev.*, 1965, **140**, A1133–A1138.

7 G. Kresse and J. Furthmüller, *Phys. Rev. B*, 1996, **54**, 11169–11186.

8 J. P. Perdew, K. Burke and M. Ernzerhof, *Phys. Rev. Lett.*, 1996, **77**, 3865–3868.

9 P. E. Blöchl, *Phys. Rev. B*, 1994, **50**, 17953–17979.

10 H. J. Monkhorst and J. D. Pack, *Phys. Rev. B*, 1976, **13**, 5188–5192.

11 S. Nosé, *Prog. Theor. Phys. Suppl.*, 1991, **103**, 1–46.

12 S. Baroni, S. de Gironcoli, A. Dal Corso and P. Giannozzi, *Rev. Mod. Phys.*, 2001, **73**, 515–562.

13 P. Giannozzi, S. Baroni, N. Bonini, M. Calandra, R. Car, C. Cavazzoni, D. Ceresoli, G. L. Chiarotti, M. Cococcioni, I. Dabo, A. Dal Corso, S. de Gironcoli, S. Fabris, G. Fratesi, R. Gebauer, U. Gerstmann, C. Gougoussis, A. Kokalj, M. Lazzeri, L. Martin-Samos, N. Marzari, F. Mauri, R. Mazzarello, S. Paolini, A. Pasquarello, L. Paulatto, C. Sbraccia, S. Scandolo, G. Sclauzero, A. P. Seitsonen, A. Smogunov, P. Umari and R. M. Wentzcovitch, *J. Phys. Condens. Matter*, 2009, **21**, 395502.

14 G. Kresse and D. Joubert, *Phys. Rev. B*, 1999, **59**, 1758–1775.

15 P. B. Allen and R. C. Dynes, *Phys. Rev. B*, 1975, **12**, 905–922.

16 F. Giustino, M. L. Cohen and S. G. Louie, *Phys. Rev. B*, 2007, **76**, 165108.

17 E. R. Margine and F. Giustino, *Phys. Rev. B*, 2013, **87**, 024505.
18 S. Poncé, E. R. Margine, C. Verdi and F. Giustino, *Comput. Phys. Commun.*, 2016, **209**, 116–133.
19 A. A. Mostofi, J. R. Yates, Y.-S. Lee, I. Souza, D. Vanderbilt and N. Marzari, *Comput. Phys. Commun.*, 2008, **178**, 685–699.
20 J. S. Tse, Y. Yao and K. Tanaka, *Phys. Rev. Lett.*, 2007, **98**, 117004.
21 D. Kasinathan, J. Kuneš, A. Lazicki, H. Rosner, C. S. Yoo, R. T. Scalettar and W. E. Pickett, *Phys. Rev. Lett.*, 2006, **96**, 047004.
22 Y. Ma, D. Duan, Z. Shao, H. Yu, H. Liu, F. Tian, X. Huang, D. Li, B. Liu and T. Cui, *Phys. Rev. B*, 2017, **96**, 144518.
23 Y. Liang, M. Xu, S. Lin, X. Yuan, Z. Qu, J. Hao and Y. Li, *J. Mater. Chem. C*, 2021, **9**, 13782–13788.
24 L. Ma, X. Yang, G. Liu, H. Liu, G. Yang, H. Wang, J. Cai, M. Zhou and H. Wang, *Phys. Rev. B*, 2021, **104**, 174112.
25 Y. Liang, X. Zhang, M. Xu, G. Xu and Y. Li, *Mater. Today Phys.*, 2022, **27**, 100817.
26 S. Han, L. Yu, Y. Liu, B. Zhao, C. Wang, X. Chen, Y. Zhang, R. Yu and X. Liu, *Adv. Funct. Mater.*, 2023, **33**, 2213377.